Article

Compression after ballistic impact response of pseudoelastic shape memory alloy embedded hybrid unsymmetrical patch repaired glass-fiber reinforced polymer composites

Luv Verma[1], Srinivasan M Sivakumar[1], Jefferson Andrew J[1], G Balaganesan[2] ⓘ, A Arockirajan[1] ⓘ and S Vedantam[3]

Abstract

This paper investigated the influence of embedding pseudoelastic shape memory alloy within the external bonded patch made up of glass fibers on the compression after impact response of adhesively bonded external patch repaired glass/ epoxy composite laminates. Unsymmetrical patch repair was employed in the current studies. Three innovative pseudoelastic shape memory alloy configurations (straight wired, meshed and anchored) were embedded inside the patch and the changes in high-velocity impact response and damage tolerance at four impact velocities (70, 85, 95, 105 m/s) were compared with the conventional glass/epoxy (glass fiber-reinforced polymer) patch. Anchored specimens showed the best response by improving the compressive strength by 25% under non-impacted conditions and restoring it by 88%, 77%, 29%, and 28% at the impact velocity of 70, 85, 95, and 105 m/s, respectively, in comparison to the conventional normal specimens.

Keywords

Composite materials, ballistic impact, compression after impact (CAI), composite repair, and external patch repair

Introduction

Marine and aerospace industries are the major ones which use parts made up of composite materials.[1–3] During their service life, aircraft or naval vessels undergo impact loading and thus have a tendency to form internal cracks.[4] One of the ways to repair such cracks is adhesively bonded patch repair. The advantages are the easy replacement, reduced machining of damaged parts, better fatigue life, lower stress concentration, high residual specific strength, and stiffness.[5–10] In some aircraft and marine structures, repairs are allowed only on one side due to inaccessibility of the other side or due to the reason which is to keep skin drag development in check.[4,11–14] Sometimes it is difficult to do patching on both sides (symmetrical patch) of the developing or propagating patch due to adhesives' thermal residual stresses.[15] Due to all these reasons, single side (unsymmetrical) patch repair is used most commonly and have been investigated by the several studies.

Investigations carried out related to patch repair constitute similar materials used to fabricate the parent laminates (i.e. mostly glass or carbon fiber). Once the external patch is adopted to repair the region which undergoes transverse loads, the patch made up of glass and carbon fibers exhibits certain drawbacks. Generally, they have low toughness and can have premature failure of the repaired region, specifically if it is having a high-stress concentration.[10,16] To overcome these issues it is required that the patch

[1]Department of Applied Mechanics, IIT Madras, India
[2]Department of Mechanical Engineering, IIT Madras, India
[3]Department of Engineering Design, IIT Madras, India

Corresponding author:
A Arockirajan, Indian Institute of Technology Madras, MSB226, Chennai 600036, India.
Email: aarajan@iitm.ac.in

should have a high strain to failure, high impact resistance, and residual strength.

One of the ways to increase the impact resistance of the external patch is by embedding pseudoelastic shape memory alloy (PE-SMA) wires in the patch. PE-SMA has the capability to undergo a higher amount of strain before deforming permanently and thus they can increase the overall toughness if embedded in the external patch. As PE-SMA can absorb a large amount of energy and have self-centric capabilities, it increases the overall ductility of the external patch, cycles of loading, and their impact resistance which makes them suitable to use in the areas of high dynamic loading.[17,18] Impact protection behavior of the SMA has been compared with that of steel under the low velocity and it was shown that SMA dissipates 2.4 times higher energy than the steel wire.[19] Another investigation was conducted to compare the impact behavior of steel and SMA wire (same diameter) embedment in composite specimens under low-velocity impact. Results indicated that steel embedment did not result in any increase in the impact response of composites.[20]

Investigations were carried out by embedding SMA in the glass fiber, carbon fiber, and graphite composites in the parent laminate under quasi-static loading, low-velocity impact, and high-velocity impact. Results have shown an increase in the energy absorption and perforation toughness of the SMA-embedded composites.[21–26] In the studies so far, researchers have used the straight-wired or bi-directional SMA configurations embedded within the composite parent laminate and have evaluated the impact resistance based on the amount of energy absorbed under impact. In such configurations, SMA matrix pull-out damage mode was predominantly noticed and this damage mode leads to low energy absorption capability. This is a concerning issue which has not been investigated in detail in the literature available. Reduction in SMA matrix pull-out damage mode can lead to further increase in the impact resistance. Generally, SMA absorbs a high amount of energy. To maximize its use in the composites depends a lot on the amount of load which can be transferred from the matrix to SMA. Thus it is important to look at the interfacial bonding properties of SMA with the matrix, as bonding affects the distribution of transverse load through SMA. Generally, the bonding of SMA/matrix interface within composites is weak. Researchers have employed surface treatment methods such as using chemicals to produce a porous oxide layer, improving wetting properties between metal and resin, and sand-blasting. These methods improve interfacial bonding to a certain extent.[10,11] But once, debonding between the two initiates, interfacial strength weakens further leading to the propagation of this debonding along the entire embedded length of SMA. Due to debonding, strain stop increasing within the embedded SMA, thus limiting the energy absorption capabilities of embedded SMA.

One of the ways to ensure that SMA reaches its maximum strain capabilities before getting pulled out of the composite sample is to modify the configuration of embedded SMA.[27,28] This can be achieved by tying knots of SMA at regular intervals within the embedment. The advantage of doing this is that SMA knots act as restrainers. Even if debonding initiates at an impact point, the configuration makes sure that it does not extend beyond a point where debonding meets the knots. Thus, a higher amount of energy is required for further pull-out. Thus, we have come up with the novel anchored configuration embedded within glass fiber-reinforced polymer (GFRP) composites. In this configuration, SMA pull-out is the least in comparison to the other two configurations (straight-wired and meshed SMA). Therefore, it increases the impact resistance as a higher amount of energy is required for further pull-out.

In the past, many studies were conducted to investigate the behavior of the laminates under compressive loads.[29–31] The major failure modes under compressive loading are local fiber micro-buckling, kinking, delamination crushing which may lead to the premature failure.[32,33] It is important to characterize the residual strength of structures such as aircraft and spatial launchers which are prone to accidental damage due to a bird strike, rock hit or hail stone impact.[34] To understand how much load a structure can withstand after such accidental damages compression after impact (CAI) test is essential to perform. Investigations done earlier in the area of CAI strength are still in the nascent stage and literature is not available on CAI strength of SMA-based external patch.

In this work, CAI response of the SMA-embedded external patch repaired specimens has been investigated. This led to the assessment of the residual strength of the laminates repaired with SMA-embedded external patch subjected to a high-velocity impact at different velocities which has not been investigated until now. There are different types of SMA embedment that were employed in the external patch. These different types of embedment have different SMA configurations. Out of these three, increase in impact resistance in terms of energy absorption and residual strength in the novel anchored SMA configuration was compared with the two other SMA configurations and with the conventional GFRP patch which was considered as a base material in the current studies. The reasons behind the increase were investigated in terms of the damage progression with respect to time during an impact event and also in terms of the additional failure modes observed due to the SMA embedment.

Experimental procedure

Materials and fabrication

Bi-directional woven roving mat glass fiber of areal density 360 g/m^2 was used as the primary reinforcement for the composite laminate preparation. Epoxy resin (LY556) and hardener (HY951) were used in the weight ratio of 10:1 as the matrix material. The properties of various material employed to fabricate the laminates were summarized in Table 1.

Six-layered glass/epoxy specimens were fabricated using the resin infusion process with curing time of 24 h under the maintained vacuum gauge pressure of 30 mm Hg at room temperature (30°C). The laminates of size 150 × 150 mm with a thickness of 3.15 ± 0.02 mm were cut out using abrasive waterjet cutting. Rectangular glass/epoxy specimens of dimension 150 × 100 mm were trimmed from different impacted glass/epoxy specimens using abrasive waterjet machining, so as to meet standard ASTM D7137M-12 for following post-impact compression tests.

SMA properties

Pseudoelastic SMA (nitinol: nickel-titanium alloy, i.e. 50 at% of NiTi) with a diameter of 0.3 mm is used as the secondary reinforcement in the external repair patch. Table 2 shows the transformation temperatures and the properties of the pseudoelastic SMA wire. Generally, the austenite finish and start temperatures determine the upper and lower plateau stress of the hysteresis (Figure 1) and the elongation to failure. Higher elongation to failure and higher ultimate failure strength is necessary for higher toughness. SMA wire used had elongation to failure strain of 1800 MPa. The maximum transformation strain was approximately 9.5–9.7% at almost constant stress of 500–520 MPa (Figure 1).

Repair technique

Preliminary high-velocity impact tests were conducted on the GFRP parent laminates at different velocities (70, 85, 95 and 105 m/s). Post-impact damage area

was measured using the scale (Figure 2). The maximum damage length in the parent laminates came out to be 14.5 ± 0.2 mm. Since circular hole provides evenly curved boundary and optimal stress pattern around the hole periphery, the irregular damage area was dressed as a circular hole. Thus, to induce damage, a 15-mm diameter circular hole was machined at the center for all the glass/epoxy specimens using abrasive waterjet machining process.

The machining was performed at a low waterjet pressure of 3400 bar to avoid delamination. Before the commencement of repair procedure, the specimens

Table 2. Properties (transformation temperatures, failure stress and maximum transformation and failure strain) of SMA wire.

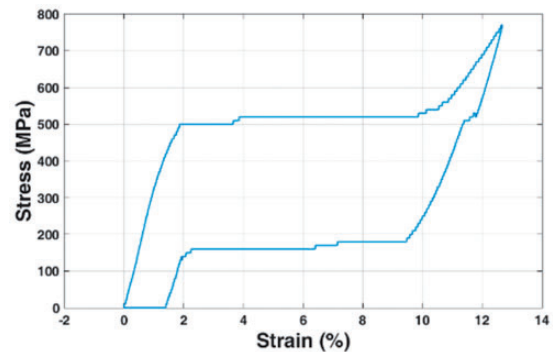| S. No.	Properties	Values
1	Austenite finish temperature (A_f)	259 K
2	Austenite start temperature (A_s)	248 K
3	Martensite start temperature (M_s)	235 K
4	Martensite finish temperature (M_f)	222 K
5	Elongation to failure	17.5%
6	Maximum failure stress	1800 MPa
7	Maximum transformation strain	9.5–9.7%

SMA: shape memory alloy.

Figure 1. Stress–strain response showing hysteresis cycle of SMA.

Table 1. Material properties of SMA, glass fiber, and epoxy.

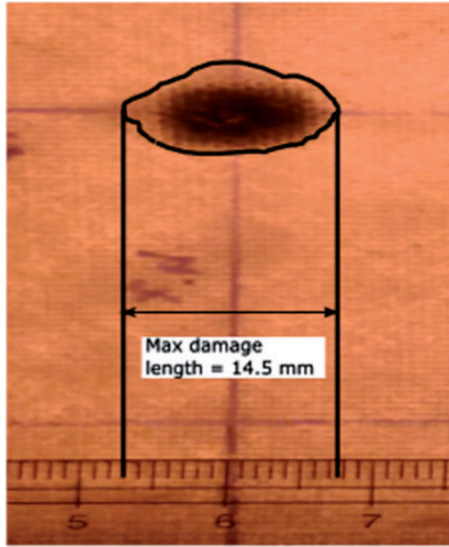| S. No.	Properties	SMA	Steel	Glass fiber	Epoxy	Units
1.	Poisson's ratio	0.3	0.3	0.25	0.30	–
2.	Density	6500	7700	2580	1200	kg/m^3
3.	Young's modulus	Austenite—80, Martensite—40	210	76.6	3.792	GPa

SMA: shape memory alloy.

Figure 2. Maximum damage in GFRP parent specimen at an impact velocity of 70 m/s.

were wiped using acetone solution to evade loosely held debris (as per standard ASTM D2093). Furthermore, to enhance bonding among the patches and the parent laminate, the specimen surface was prepared applying sandpaper (200-grit). The repair process was performed with the aid of a resin infusion technique with curing time of 24 h under the maintained vacuum gauge pressure of 30 mm Hg. SMA-embedded glass/epoxy square patches with sides of length 35 mm were then bonded externally over the surface of the damaged region (Figure 3). Square patches were employed to get the equal bonding region along all four edges of the patch. Both the parent laminate and external patches were fabricated using fabrics of the same fiber architecture and thickness. The properties of glass fiber, and epoxy to fabricate the patch were given in Table 2.

Four different types of the external patch were fabricated. Their configurations were conventional GFRP, straight-wired SMA, meshed SMA, and anchored SMA as shown in Figure 3. In the first configuration,
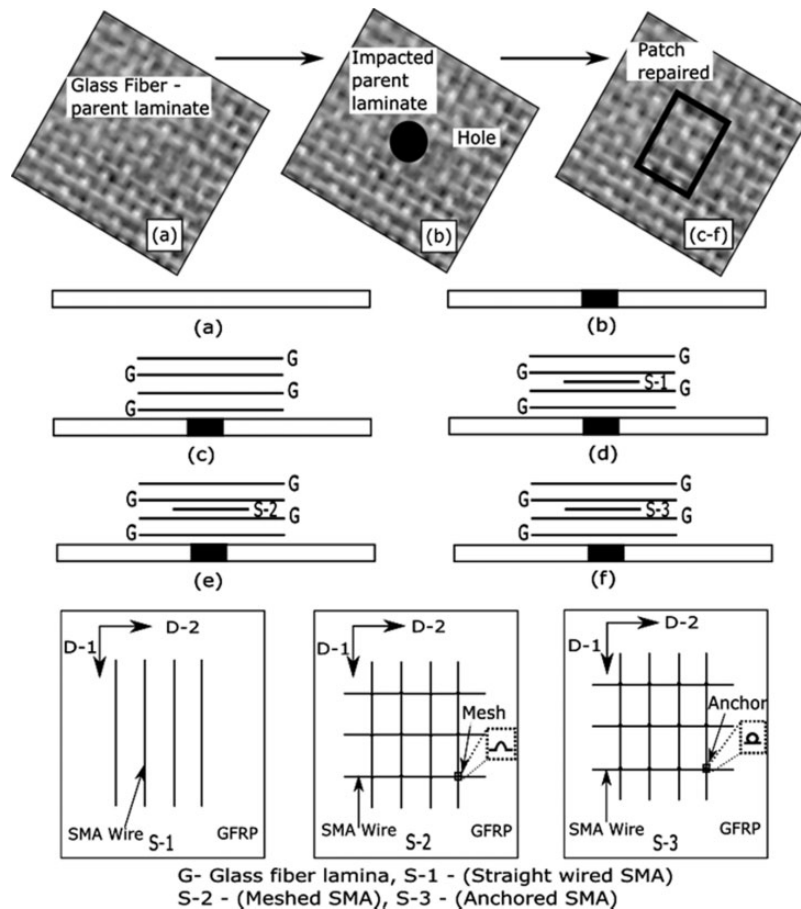

Figure 3. Schematic diagram of different specimens (a) GFRP parent, (b) damaged, specimen repaired using (c) GFRP, (d) straight-wired SMA, (e) meshed SMA, and (f) anchored SMA-based patches.

specimens were fabricated using only glass fiber and epoxy matrix. In the second (straight wired) configuration, four independent SMA wires of length 30 mm were embedded in between the middle GFRP layers as an embedment. In the third (meshed) configuration, a mesh of SMA wires or woven SMA wires was embedded in between the middle GFRP layers. In direction 1 (D-1), wires of length 30 mm were laid, then they were weaved or meshed by SMA wire from the perpendicular direction named as D-2. Similarly, last (anchored) configuration was also embedded in between the middle GFRP layers. In this configuration, SMA wires were laid in D-1 and they were anchored by SMA in D-2 with the help of tying knots around SMA in D-1 as shown in Figure 3. Nominal distance between the wires in both directions was maintained to be 4 mm, which had to be less than the projectile's diameter (8 mm).

Respective volume fractions of the SMA content in the straight wired, meshed, and anchored configurations were 3.10%, 4.84%, and 5.21%. Codes for different SMA-embedded glass/epoxy patch were summed up in Table 3.

Throughout the paper, specimens repaired with normal GFRP external patch were considered as the standard for the comparison of CAI properties and failure profiles.

Multiple quasi-static indentation tests

According to ASTM standard D6264-98(04), quasi-static multiple indentation tests were carried out using Tinus Olsen Universal Testing Machine (UTM) of maximum load capacity 100 kN. Four corners were clamped tightly with the help of toggle clamps as shown in Figure 4. Incremental displacement steps of 2, 4, 6, 8, 10, and 12 mm were applied one after the other from the point where the indenter initially contacted the specimens. The feed rate was set as 1 mm/min.

High-velocity impact test

To determine the impact velocities, preliminary impact tests were conducted to find out the ballistic limit of the patch repaired specimen embedded with the novel anchored SMA configuration. Two velocities below and two velocities above the determined ballistic limit were chosen to compare its impact resistance at those velocities with the other two SMA-embedded configurations and GFRP patch-repaired specimens using an in-house build gas-gun set-up (Figure 5) to induce impact damage. These velocities were 70, 85, 95, and 105 m/s and their corresponding incident energies were 19.6, 28.9, 36.1, and 44.1 J. The target laminates were clamped from all four sides. For each energy level, five specimens were tested and their average was used for interpretation. A projectile of diameter 8 mm and mass 8 g was used to impact the clamped specimens. While impact, two high-speed cameras of Phantom make, model V611 at 50,000 fps were used. One camera was used to measure the projectile velocity and energy absorption. Another camera was used to capture the progression of failure or damage modes.

During the event of impact control setting was done such that bullet hits at the knot, so number of wires participating and their configuration played an important role instead of their orientation as impact is a transverse loading. SMA wire of 0.3 mm diameter was used
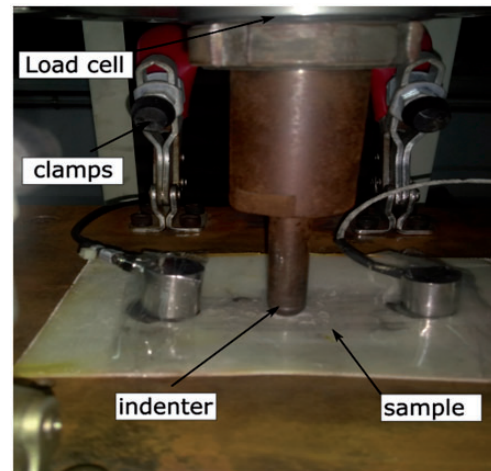

Figure 4. Specimen clamped in ASTM D 6264-98 indentation fixture.

Table 3. Code for different glass/epoxy specimens.

S. No.	Configuration	SMA connection type	Nomenclature
1	Glass/epoxy (GFRP)	–	GFRP
2	Independent straight wires	Independent	Straight-wired SMA
3	Meshed straight wires	Laid as woven SMA	Meshed SMA
4	Anchored straight wires	SMA knot points	Anchored SMA

GFRP: glass fiber-reinforced polymer; SMA: shape memory alloy.
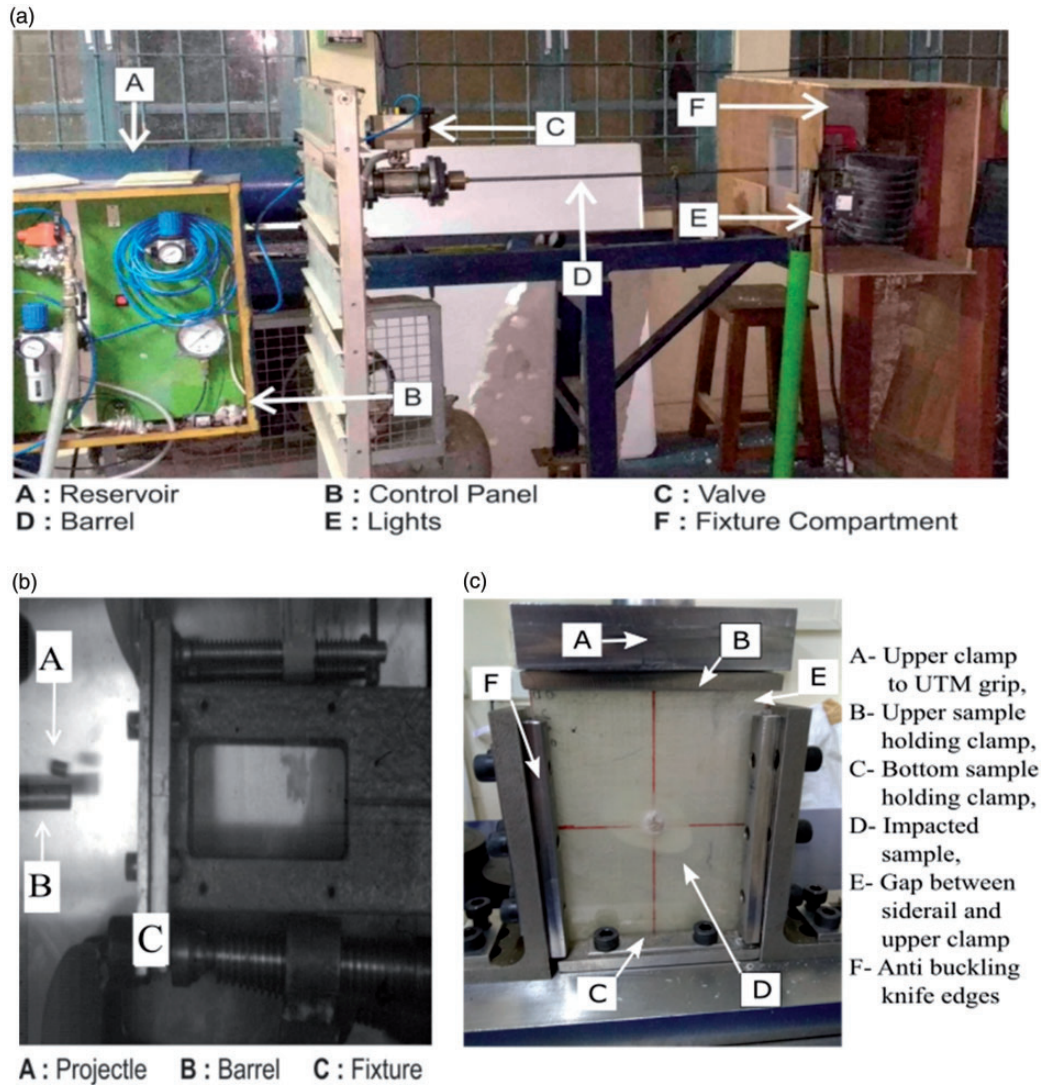
Figure 5. (a,b) High-speed gas gun set-up, (c) compression after impact (CAI) test set-up.

as an embedment. Increase in wire diameter can lead to further increase in the energy absorption as volume of the wire coming in contact with impactor will increase, but it leads to other issues such as increase in the SMA volume fraction in the patch making them heavier and can also lead to debonding and surface non-uniformities.

Compression after impact

CAI tests were conducted on both repaired impact and repaired non-impacted specimens to find out the residual compressive strength and to characterize the failure modes. Figure 5 shows the placement of the CAI specimen in the ASTM D7137-12 CAI fixture. Tests were carried out in 50 kN maximum load capacity INSTRON 8801 UTM. According to ASTM D7137 a cross-head speed of 1 mm/min was maintained.

Results and discussion

Energy absorption and damage progression

Preliminary multiple indentation tests were carried out on the GFRP specimens embedded with steel wires (anchored configuration). Same multiple indentation tests were performed on the anchored SMA configuration.

It was found that the ultimate failure load was the highest for steel embedment (1430 N) up to 3rd cycle, but its ultimate failure displacement was only 5.33 mm in comparison to anchored SMA configuration which was 10 mm. Also, for steel embedment maximum cycles to failure were three (Figure 6(a)), whereas it was five for SMA-embedded composite specimens (Figure 6(b)). Though, ultimate failure load was higher for steel wire embedment up to 3rd cycle, steel wire underwent permanent deformation earlier
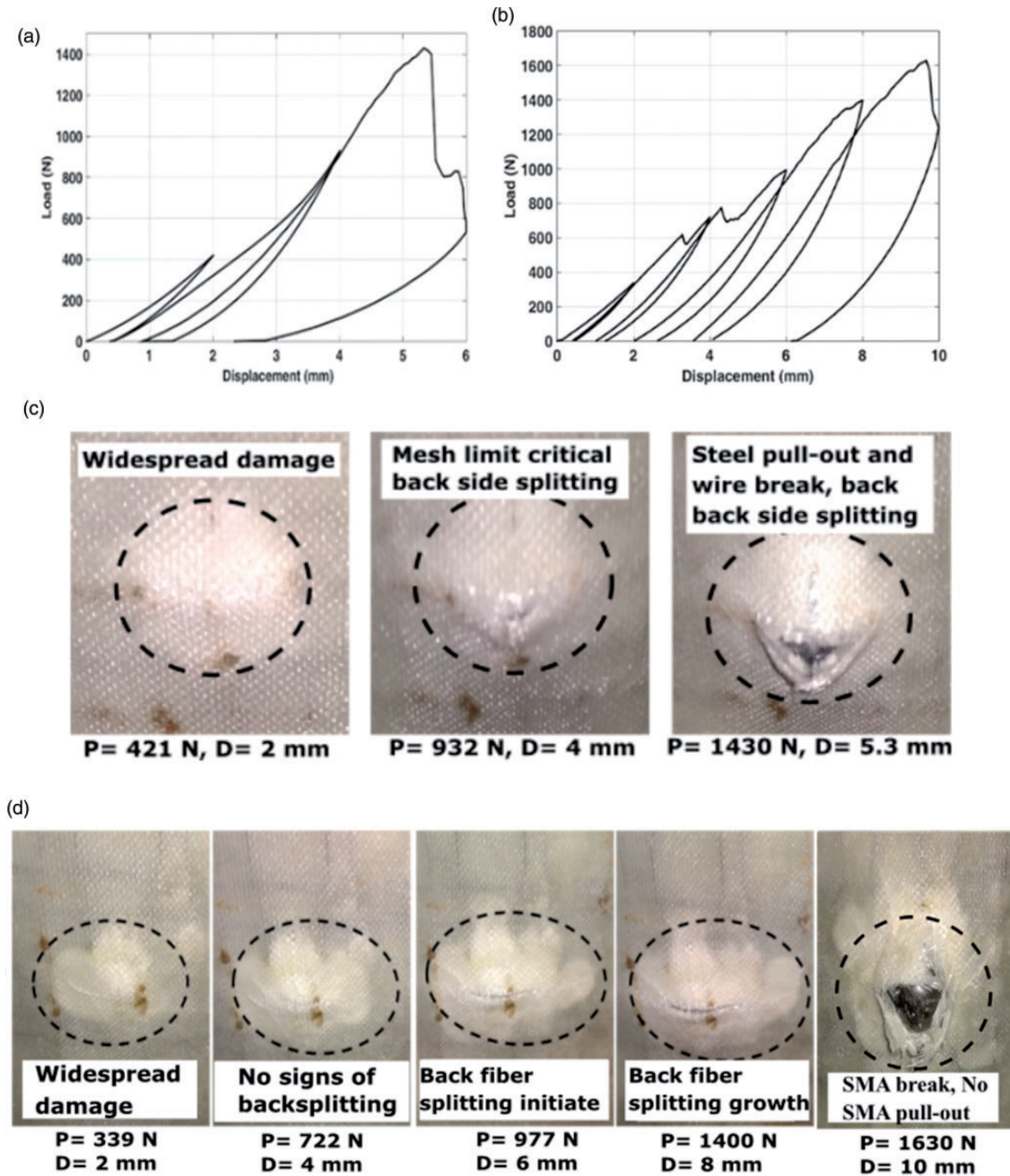
Figure 6. Preliminary test results on steel embedded glass/epoxy specimens showing (a) force–displacement curves, (b) indentation load, AE cumulative counts and AE event location vs. time curves and (c) photographic images of fractured steel embedded GFRP specimens and (d) photographic images of SMA-embedded GFRP specimens at various indentation cycles.

than SMA wire. Once it underwent permanent deformation in the impact zone, steel anchors did not play any role in the energy absorption and further increase in the indenter load led to the fracture of steel wire (Figure 6(c)), leading to ultimate failure of the entire specimen. SMA wire was able to sustain the load due to its capability to undergo higher strains and reached the ultimate failure load of 1630 N in the 5th cycle (Figure 6(b,d)).

Thus, from the literature[19,20] and from the above investigation (Figure 6), after establishing that SMA toughness is higher than steel, assessment of the impact response of SMA-embedded composite specimens was investigated.

To evaluate the high-velocity impact damage on laminated composites, it is well-known to refer to the absorbed energy parameter.[35] The kinetic energy of the projectile before contact with target is referred to as

impact energy, whereas absorbed energy is the energy transferred to the target by various damage modes occurring after the projectile contact, like fiber pull-out, fiber fracture, fiber/matrix debonding, adhesive or cohesive failure, matrix cracking, and interlaminar delamination[36] and is calculated by finding out the difference between the initial kinetic energy before impact and residual kinetic energy after impact. The absorbed energy depends on nature and extends of the failure. Also, the absorbed energy is directly linked to the impact resistance. Increase in the impact resistance of the sample will lead to an increase in the energy absorption.

After evaluating the speed of the impactor before and after impact with the help of a high-speed camera, the absorbed energy was plotted against the impact velocity for various specimens (Figure 7). It can be evidently noticed that the impact behavior changed significantly with the architecture of the SMA wire embedded in the external patch of repaired specimens and the impact velocity. Figure 7 implied that the perfect elastic rebound of the projectile did not occur for any of the specimens. Consequently, the kinetic energy of the projectile was transferred to the specimen for the contact duration of the projectile and was absorbed in the initiation and progression of damages.

At all the impact velocities, normal GFRP specimens depicted the least energy absorption, whereas, anchored specimens illustrated the highest energy absorption. Specimens embedded using meshed and straight-wired SMA absorbed the impact energy intermediate between normal and anchored specimens. In specific, normal and various SMA-based specimens can be sorted from lower to higher energy absorption in the following order: normal < straight-wired < meshed < anchored. However, the difference in absorbed energy between

various specimens at various impact velocities is significantly different. At higher impact velocities, absorbed energy tended to be highly reliant on the architecture of SMA embedment in the external patch, because the increase in impact resistance depended a lot on SMA architecture within the patch. This obviously highlighted that with raising impact velocity, failure mechanisms responsible for the absorption of applied impact energy varied.

Starting from the impact velocity of 70 m/s, normal and straight-wired specimens showed a different response. They were characterized by a decreasing trend of absorbed energy among various specimens. For meshed specimens, the absorbed energy increased with increasing impact velocity up to 85 m/s. The post-impact velocity of 85 m/s, a sharp decrement in the absorbed energy was observed. Until up to impact velocity of 95 m/s, anchored specimens were the only ones that absorbed the significantly higher amount of impact energy in comparison to the other specimens, as they depicted almost saturated or reducing behavior as they reached their ultimate energy absorption capabilities. This highlights the improvement in the impact response (in terms of increase in energy absorption) of patch-repaired specimens embedded with the anchored configuration over all the other configurations. The reasons for all these observations were explained by using absorbed energy progression, contact duration, and damage progression of various glass/epoxy specimens under high-velocity impact loading in the following sections.

Figure 8(a,b) shows the stages of projectile movement in the penetrating as well as rebounding specimens. These stages were 0%, 10%, 30%, 50%, 70%, and 100%, respectively. These stages of the projectile movement were normalized according to the projectile end or tail movement with respect to its initial position at 0% penetration. At 100% of projectile movement, either projectile may penetrate the specimen for penetrating specimens (Figure 8(a)) or may have rebounded from the rebounding specimens (Figure 8(b)). It was done to compare the amount of energy absorbed at each stage by penetrating as well as rebounding specimens with respect to the time at the impact velocities of 70, 85, 95, and 105 m/s, respectively. These stages were referred to as a projectile movement in further explanations.

Figure 9(a–d) shows the energy absorption versus time plot for normal and various SMA-based GFRP specimens at respective stages of the projectile movement, impacted at velocities 70, 85, 95, and 105 m/s, respectively, for rebounding and penetrating specimens. For impact velocity of 70 m/s and projectile movement of 10%, both the normal and all the SMA-based specimens showed almost similar contact duration.
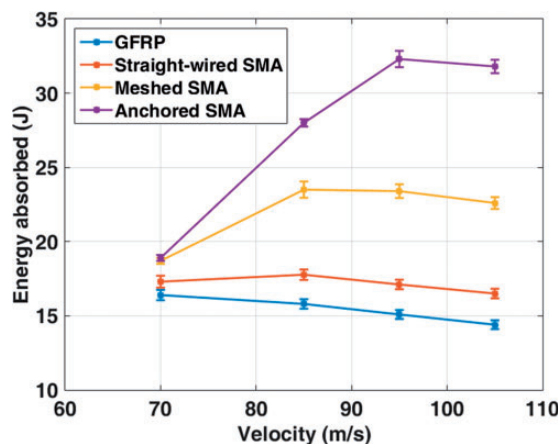

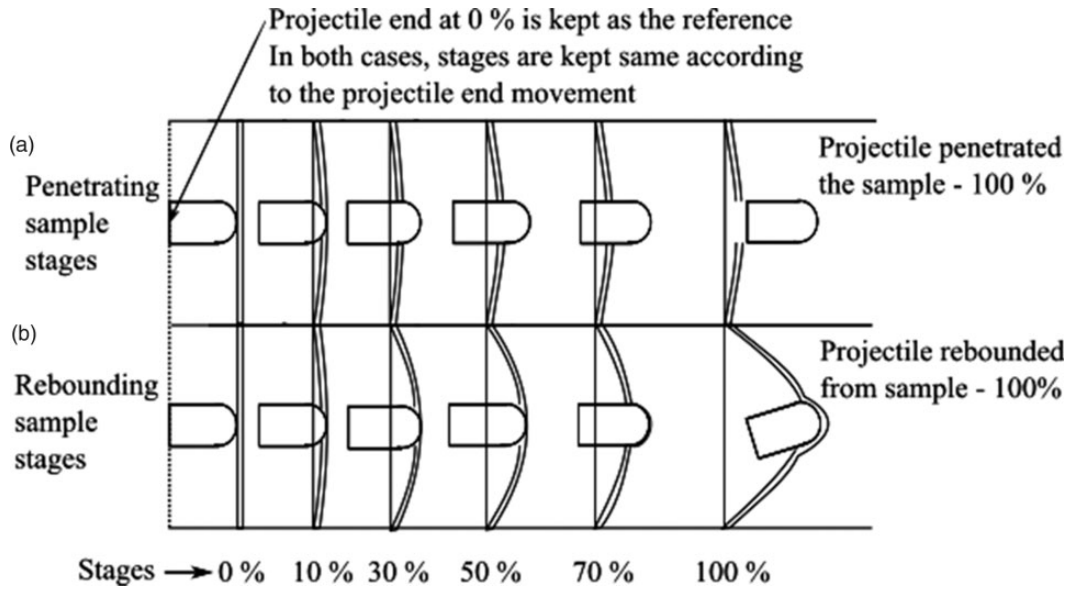**Figure 7.** Energy absorbed vs. velocity curves for different types of patch at four different velocities.

Figure 8. Schematic diagram of projectile motion stages for both (a) penetrating sample and (b) rebounding sample.
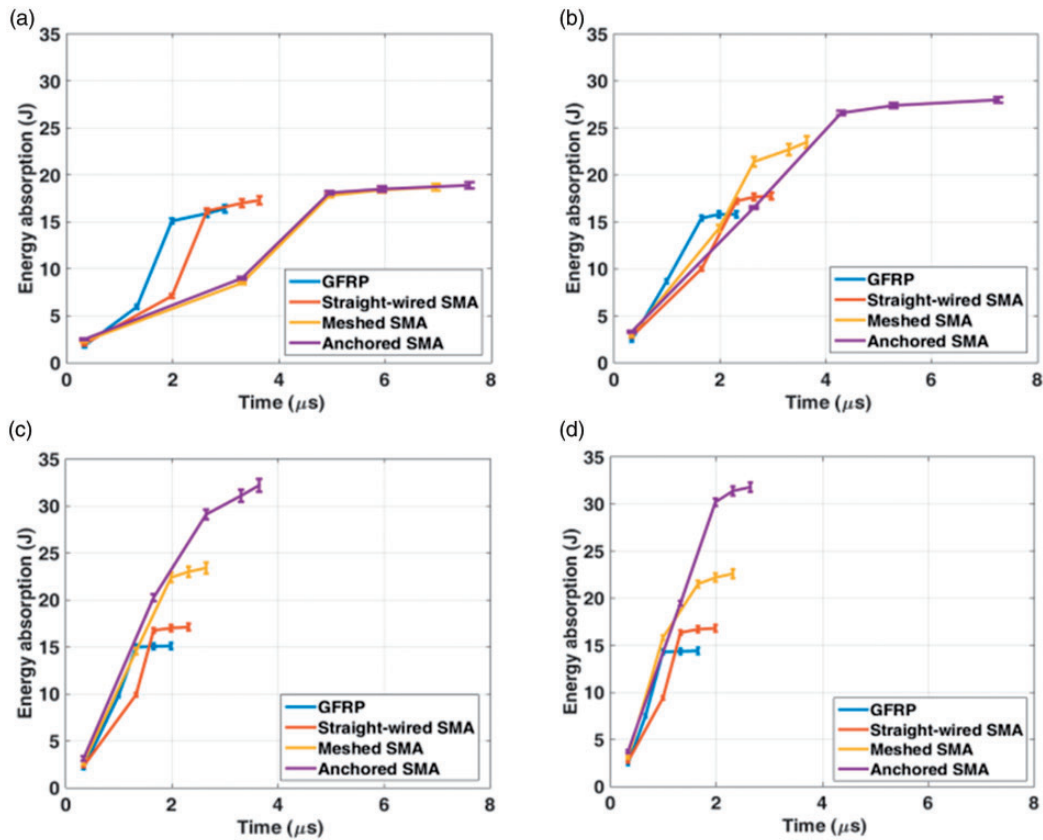

Figure 9. Energy absorption vs. time curves at five different stages of damage progression of different specimens at four different velocities: (a) 70, (b) 85, (c) 95, and (d) 105 m/s.

The difference in impact performance in terms of absorbed energy and contact duration among various specimens was considerably low at 10% of the projectile movement. However, the anchored specimens showed the maximum absorbed energy, whereas, normal specimens offered the least absorbed energy. At 10% of projectile movement, this marginal difference meant that, though largely energy absorption was

done by glass fibers failure modes initially, for anchored specimens, SMA property of higher strain to failure came into effect, leading to the initiation of enduring the impact load in a ductile manner. This led to an increase in the energy absorption. Straight-wired and meshed specimens exhibited a response between normal and anchored specimens. Also, it can be noticed in Figure 8(a–d) that, for projectile movement of 10%,

the trends of absorbed energy and contact duration for all the specimens at impact velocities of 85, 95, and 105 m/s were same as the impact velocity of 70 m/s.

At an impact velocity of 70 m/s, after projectile movement up to 30%, contact duration of normal specimens increased marginally to offer ultimate absorbed energy and resulted in complete penetration (Figure 10), depicting poor impact response among all
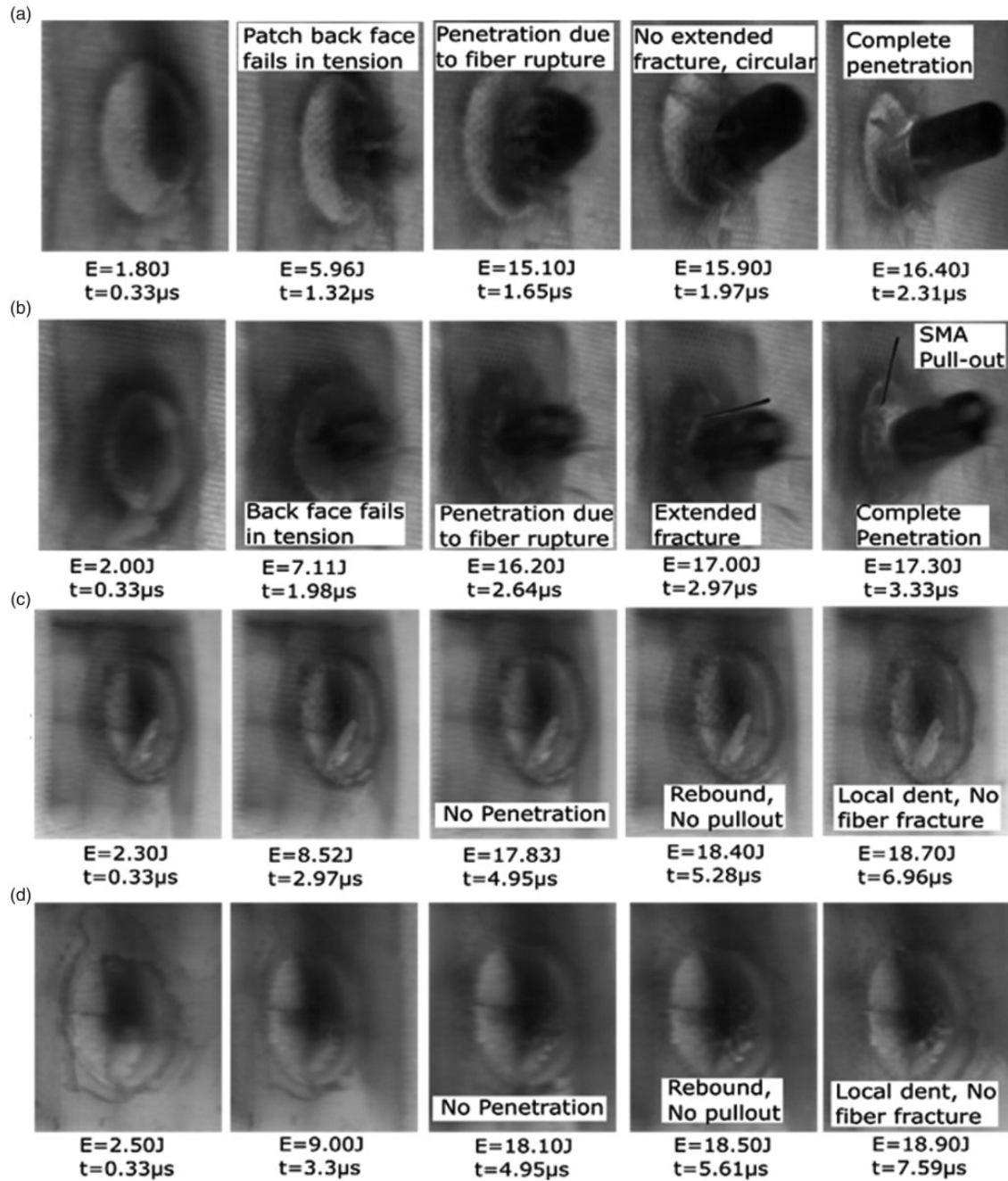

Figure 10. High-speed camera images (rear view) at five different stages of damage progression and their corresponding absorbed energy (*E*) of different specimens: (a) GFRP, (b) straight-wired, (c) meshed, and (d) anchored impacted at 70 m/s.

the repaired specimens. This response was attributed to the characteristic energy absorption mechanism of brittle glass fibers in normal specimens,[36] which dissipated the impact energy by premature breakage of glass fibers beneath the spot of application of impact loads, as clearly confirmed by the high-speed camera images (Figure 10). These results could make clear why normal specimens showed least absorbed energy. Another possible explanation for this response was that, in the case of specimens repaired using SMA wires both SMA and fibers system control the penetration of the projectile by various additional energy absorbing mechanism, whereas in the case of specimens repaired using homogeneous glass fibers had insignificant control on the projectile penetration.

However, at an impact velocity of 70 m/s, the absorbed energy versus time curve of normal specimens was nearly similar to that of the straight-wired specimens. More specifically, the difference between normal and straight-wired specimens in terms of absorbed energy and contact duration at 10%, 30%, 50%, 70%, and 100% projectile movement was considerably low. It can be seen in Figure 10 that the straight-wired specimens showed complete penetration at low absorbed energy and contact duration (i.e. near to normal specimens) than other SMA-based specimens.

For straight-wired SMA specimens, each wire acted as a separate system (Figure 17(b), side-view). Thus, for better energy absorption it is important that wire should be present beneath the impact area as SMA enhanced the impact resistance. The load carrying capability of this specimen increased until bond between a particular wire and matrix system is intact. The bonding of other wire which is not directly under load did not play any role in energy absorption. As a result, once the SMA-matrix debonding occurred in straight-wired specimens, damage at the impact site (Figure 14(b), after impact), showed that it tended to encourage the glass fibers to completely withstand the rear side tensile stress, which resulted in the premature ultimate failure (Figure 10(b)). Thus, after debonding of a single wire, impact failure modes were similar to that of normal specimens and hence straight-wired configuration does not increase the impact resistance considerably.

After the projectile movement of 50%, a considerable increment in the slope of the energy absorption versus time curve was noticed for normal and straight-wired specimens in comparison to meshed and anchored specimens at an impact velocity of 70 m/s (Figure 9(a–d)). The reason behind this observation was that, for normal and straight-wired specimens, the projectile movement of 50% resulted in penetration leading to critical fiber fracture damage mode (Figure 10(a)), which led to higher energy absorption. On the other hand, in the case of meshed and anchored

specimens, a local dent was observed in the primary impact site without any critical fiber fracture (Figure 10(c,d)). Quite contrary to the straight-wired specimens, by embedding the SMA wires in meshed and anchored architecture pattern into the external patches, it yielded superior resistance to projectile penetration for all stages of projectile movement (Figure 10(b–d)). Moreover, a similar absorbed energy versus time curve pattern was noticed among meshed and anchored specimens.

Meshed configuration acted as an improvement over a straight-wired configuration. As said earlier in straight wired configuration, only wire under the impact point improved the impact resistance, but in a meshed SMA configuration, the load acting on the wire at an impact point was distributed with the help of the mesh to other embedded wires also, which led to an increase in energy absorption (Figure 17(c), top-view). Thus other wires which were not directly under the impact load also played an important role in load. This also led to the reduction of the effect of SMA matrix debonding at the point of impact which led to an increase in the impact resistance. Because quite contrary to the straight-wired specimens, even if debonding took place at the impact site, meshed configuration still continued to absorb energy through the surrounding SMA wires. Also, at 70 m/s, there was a local dent which can be seen on the tensile or back face (Figure 10(c)), but pull-out was restricted, which was not the case with the straight-wired specimen at 70 m/s. Thus, it showed a better impact resistance than straight-wired configuration.

Anchored specimens can be considered as a combination of meshed specimens with knots. These meshes were able to restrict the penetration of indenter and delayed the critical fiber fracture (Figure 10(d)), unlike the normal and straight-wired specimens at all percentage of projectile movement, in addition to which knots further strengthened the GFRP and SMA bond by providing anchors at the knotting point (Figure 16(a), before impact) which controlled the premature pull-out of anchored SMA and further hold it in a position. As a result at 70 m/s, there was a local dent which was observed at the back face and failure mode was similar to that of meshed configuration (Figure 10(d)). This suggested that for complete perforation of the specimens, the applied impact velocity had to rise further, highlighting the superior toughness property. Hence, the ultimate contact duration at an impact velocity of 70 m/s was significantly higher for the meshed and anchored specimens rather than the normal and straight-wired specimens.

For meshed specimens, at an impact velocity of 85 m/s and after projectile movement of 50%, there was a considerable increment in the slope of the

energy absorption versus time curve and a considerable decrease in the contact duration in comparison to 70 m/s (Figure 9(a,b)). This response owed to the reason that, in meshed specimens, the impactor extremely penetrated the specimen (i.e., predominant fiber breakage accompanied with the SMA pull-out in two directions at the impact point was observed; Figure 15(b), after

impact). Photographic images of damaged specimens depicted that the ultimate failure of meshed specimens did not only occur by locally concentrated damage.

Critical debonding between SMA wire and matrix system resulted in higher stresses in the glass fibers thus leading to premature failure of meshed specimens (Figures 11(c) and 16(b), after impact and
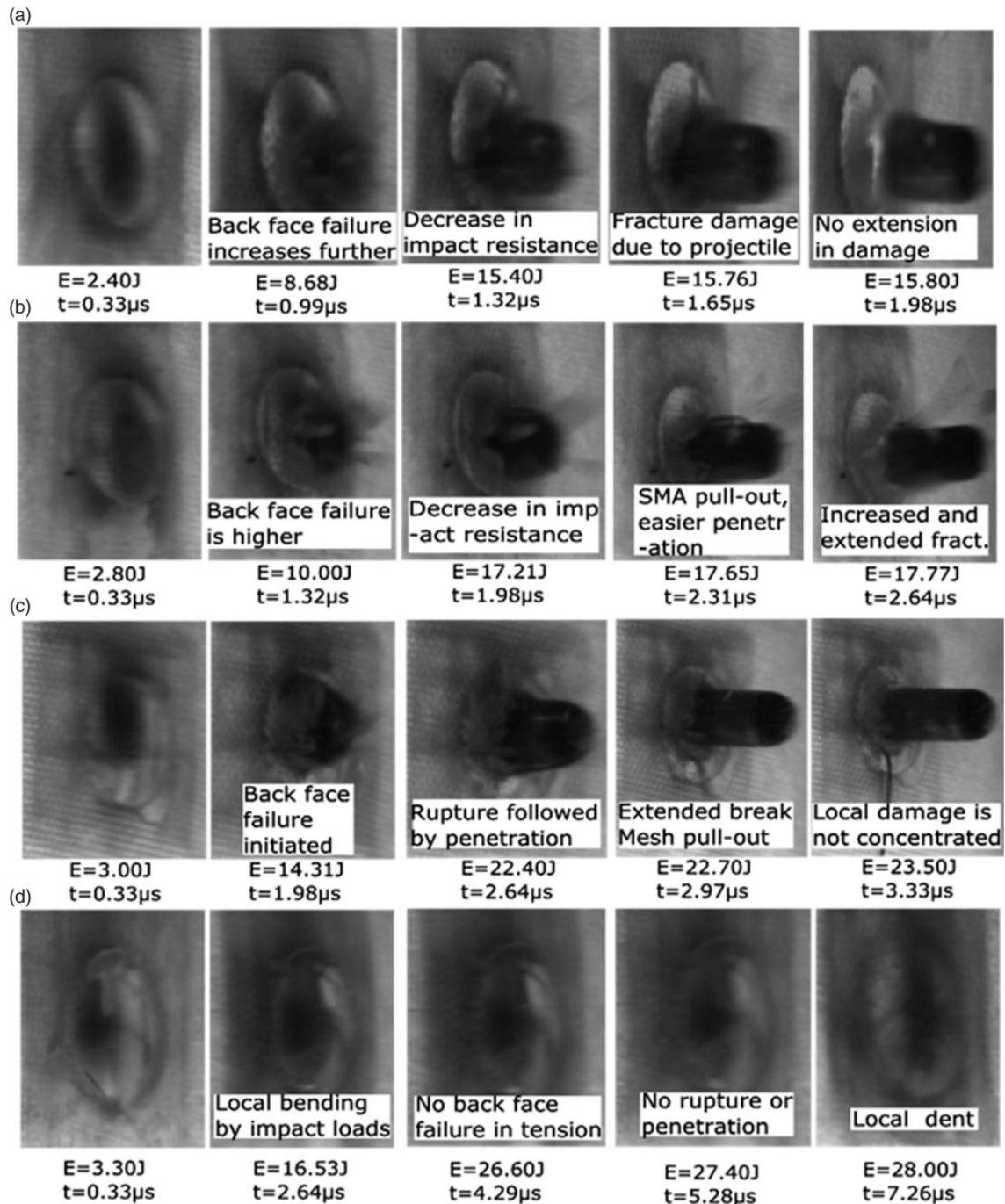

Figure 11. High-speed camera images (rear view) at five different stages of damage progression and their corresponding absorbed energy (*E*) of different specimens: (a) GFRP, (b) straight-wired, (c) meshed, and (d) anchored impacted at 85 m/s.

Figure 17(c)). In addition, at an impact velocity of 85 m/s and after projectile movement of 50% leading to the penetration, there was a gradual decrement in the slope of energy absorption versus time curve for normal and straight-wired specimens in comparison to that at 70 m/s (Figure 10(b)). This attribute owed to the increase in projectile velocity and a corresponding decrease in the contact duration.

At an impact velocity of 95 m/s and after the projectile movement of 50%, the slope of the energy absorption versus time curve was increasing significantly for anchored specimens than at earlier impact velocities. At this impact velocity, the predominant occurrence of SMA fracture (Figure 12(b)) might have resulted to encourage the brittle glass fiber layers to tolerate the complete impact stress, thus resulting in fiber failure. To be specific, in the case of anchored specimens, as explained before knots further strengthened the GFRP and SMA bond by providing anchors at the knotting points (control the premature pull-out of SMA wires) and further hold it in position (Figure 17(c), top-view and Figure 17(b), before impact). When anchored specimen underwent impact, the first knot at the impact site underwent failure. As anchored SMA now free of knot started deforming, surrounding knots started playing a major role in keeping the SMA wire in position and did not allow it to debond or any premature SMA pull-out (Figure 17(c),

side and top-view). As a result, as SMA pull-out was not allowed by other knots, this anchored SMA underwent tensile failure (fracture) at the impact point (Figure 16(b), after impact). As a result, the entire specimen was perfectly involved in the ultimate fracture process. Among various SMA-based specimens, anchored specimens were the only one to fail at higher impact velocity (Figure 12(b)) with a display of local elongation until SMA fractured. Thus, anchored specimen showed much higher improvement in energy absorption (Figure 6) and impact resistance (Figure 16(b), after impact and Figure 17(d), side-view), whereas all other specimens containing SMA wires showed a considerable pull-out and debonding of SMA from the matrix (Figures 14 and 15(a,b)) and Figure 17(b,c), side-view). These failure events, as a result, caused a significant increase in the slope of anchored specimens.

At an impact velocity of 105 m/s, the slope of the energy absorption versus time curve for anchored specimens after 50% projectile movement decreased than at earlier impact velocity (95 m/s; Figure 9(d)). Similarly, it decreased for all the other types of specimens also. This happened because, after ballistic limit (i.e. complete penetration), as impact velocity further increased, there was a decrease in the contact duration especially after 50% of projectile movement leading to specimen penetration (Figures 9(d) and 13(b)).
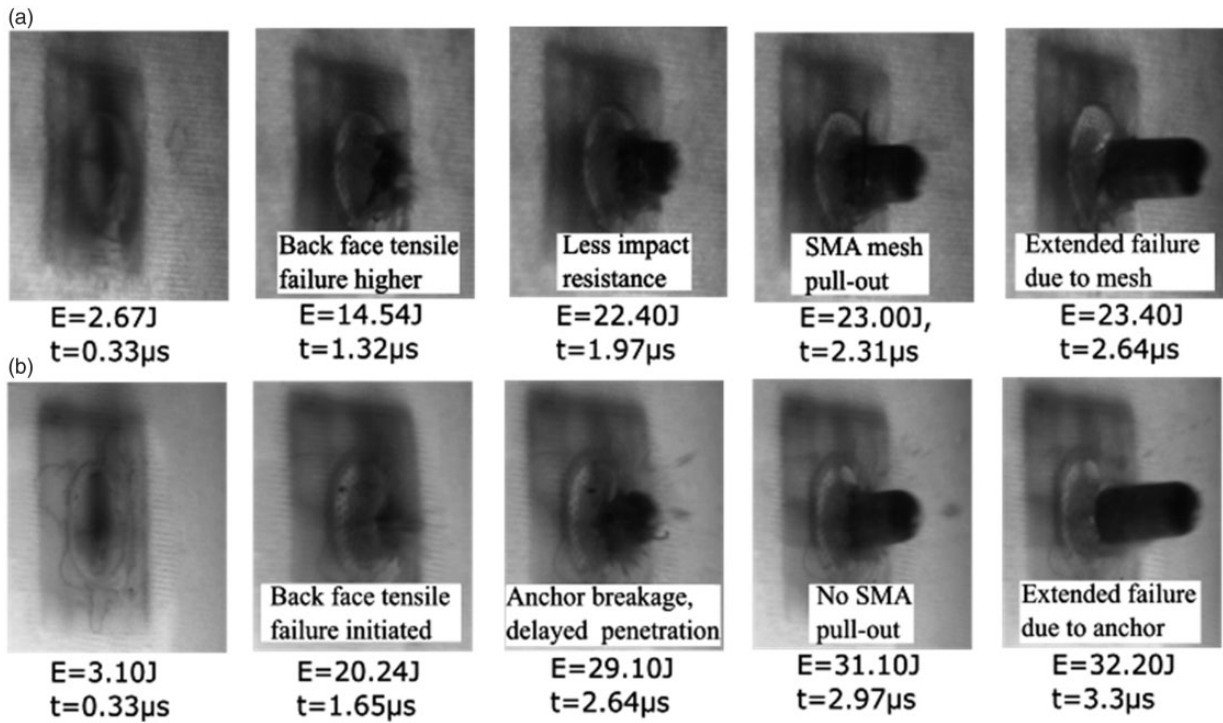

Figure 12. High-speed camera images (rear view) at five different stages of damage progression and their corresponding absorbed energy (E) of different specimens: (a) meshed and (b) anchored impacted at 95 m/s.
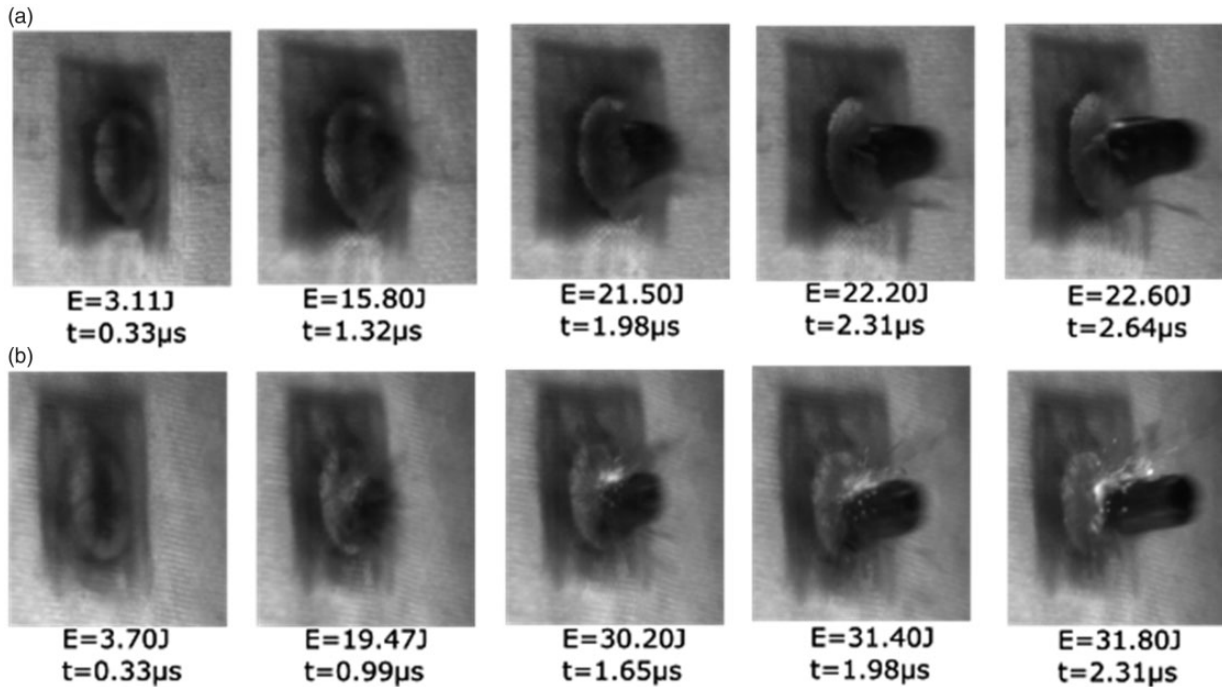
Figure 13. High-speed camera images (rear view) at five different stages of damage progression and their corresponding absorbed energy (*E*) of different specimens: (a) meshed and (b) anchored impacted at 105 m/s.

Overall, the results pointed out that embedding the SMA wire in the anchored pattern made the progression of premature fiber fracture difficult under impact loading (Figures 10, 11). At higher impact velocities, anchored specimens showed the excellent balance among fiber breakage and SMA/matrix pull-out (Figure 16(b), after impact and Figure 17(d), side-view). The positive role played by knots on anchored specimens on the local bending response is apparent in comparison to other SMA configurations (Figures 14–16(a,b), after impact and Figure 17(b–d), side-view). More specifically, specimens embedded with SMA wires which are anchored using knots (anchored specimens) provided the most optimistic drift as it illustrated the greater damage resistance. These remarks can give details why anchored specimens revealed the superior impact response than all the other specimens.

Mechanics of SMA in the anchored configuration

So far, results have established that the energy absorption is the highest in the anchored configuration (Figures 7 and 9(d)), in comparison to the other two SMA configurations (straight-wired and meshed). In the previous section, it was already discussed that SMA was better in comparison to the conventional metal such as steel because of its high toughness. In this section, why anchored specimens showed a superior behavior is established.

It can be observed from the SEM image of the post-impacted anchored configuration, that SMA wire embedded in anchored configuration underwent fracture. SMA wire employed for the impact testing were such that they had high elongation to failure and high ultimate strength (Table 2) which led to increase in overall toughness. Thus, from Table 2 and Figure 18, it can be said that SMA wire in the anchored configuration had to undergo ultimate failure strain of 17.5%. Also, fracture is the ultimate failure stage and before that SMA would have undergone initial martensitic transformation followed by plastic yielding.

To find out the exact stress–strain behavior of SMA under same strain rate as it underwent during the impact was out of scope of this study, but to calculate the amount of energy absorption due to fracture of the anchor, multiple-quasi static indentation test was carried out. Fracture energy of SMA for the indentation was approximately 8 J (Figure 6(b)). It is also well known that the energy absorption at the high-velocity impact is higher than that absorbed in the quasi-static indentation tests.[37–39] Thus 8 J is the lower bound of the amount of energy absorbed due to the SMA fracture.

Compression test

SMA architecture pattern influenced the compression behavior of repaired composite laminates both before and after impact. Figure 19 illustrated the force versus
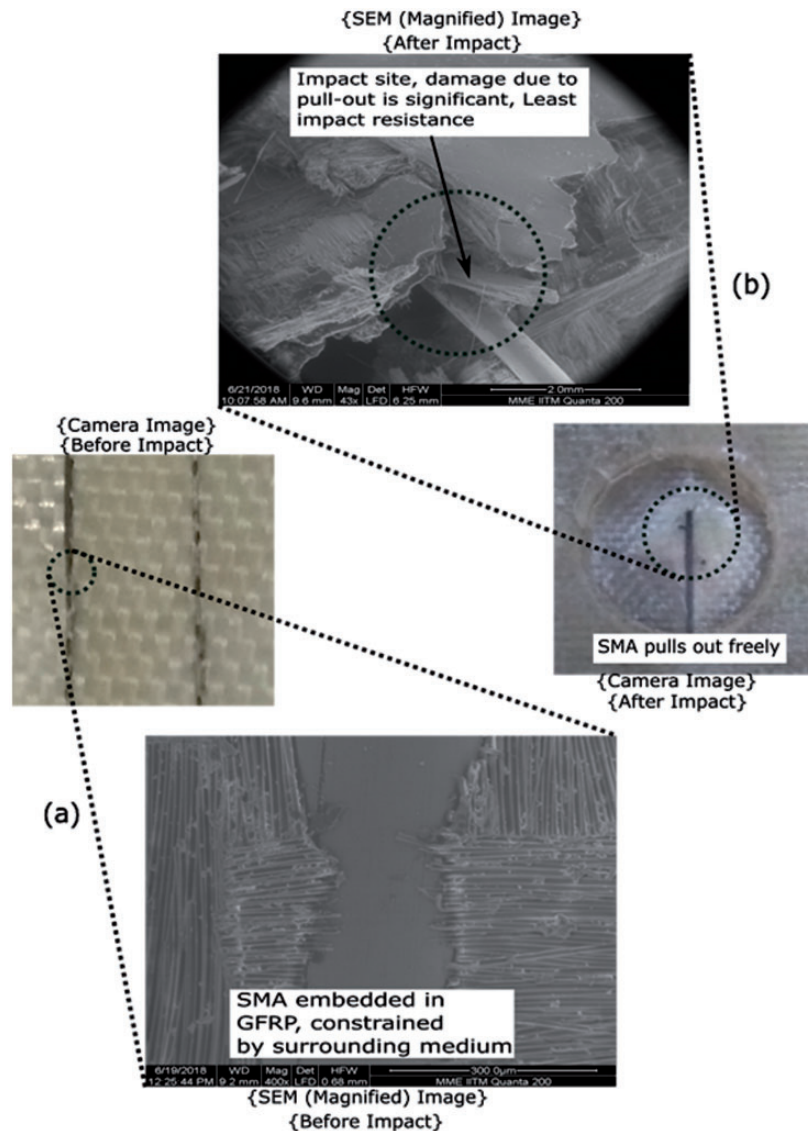
Figure 14. Straight-wired SMA-embedded patch repaired specimen showing (a) interaction between the wire and the matrix before impact and (b) damage modes after impact at the impact site using camera and SEM images.

displacement plot for non-impacted normal and different SMA-based repaired specimens. Normal specimens showed high initial stiffness whereas anchored specimens showed the least stiffness. Specimens fabricated with straight-wired and meshed SMA wires had initial stiffness intermediate between normal and anchored specimens. In specific, different repaired glass/epoxy specimens can be ranked from higher to the lower initial stiffness in the following order: normal > straight-wired > meshed > anchored.

SMA embedment offered improved balance among ultimate compressive load, toughness, and ultimate displacement to failure among the repaired specimens (Figure 19). Repairing the damage glass/epoxy specimens using straight-wired, meshed, and anchored external patches restored the ultimate compressive load by 6.1%, 13.8%, and 25%, respectively, in comparison to the conventional normal specimens. The reasons for these results are described by correlating compression properties and damage profile of different specimens in the subsequent section.

Observations of surface fracture. The key phase in analyzing the performance of repaired laminates is to characterize the profile of the failure occurred in the fractured specimens. Figure 20 illustrates the photographic image of the failure profile for various repaired specimens. By and large, a major failure is generated in the mode of adhesive or cohesive failure and fiber micro-buckling (Figure 20(a–d)). It is illustrious that, under
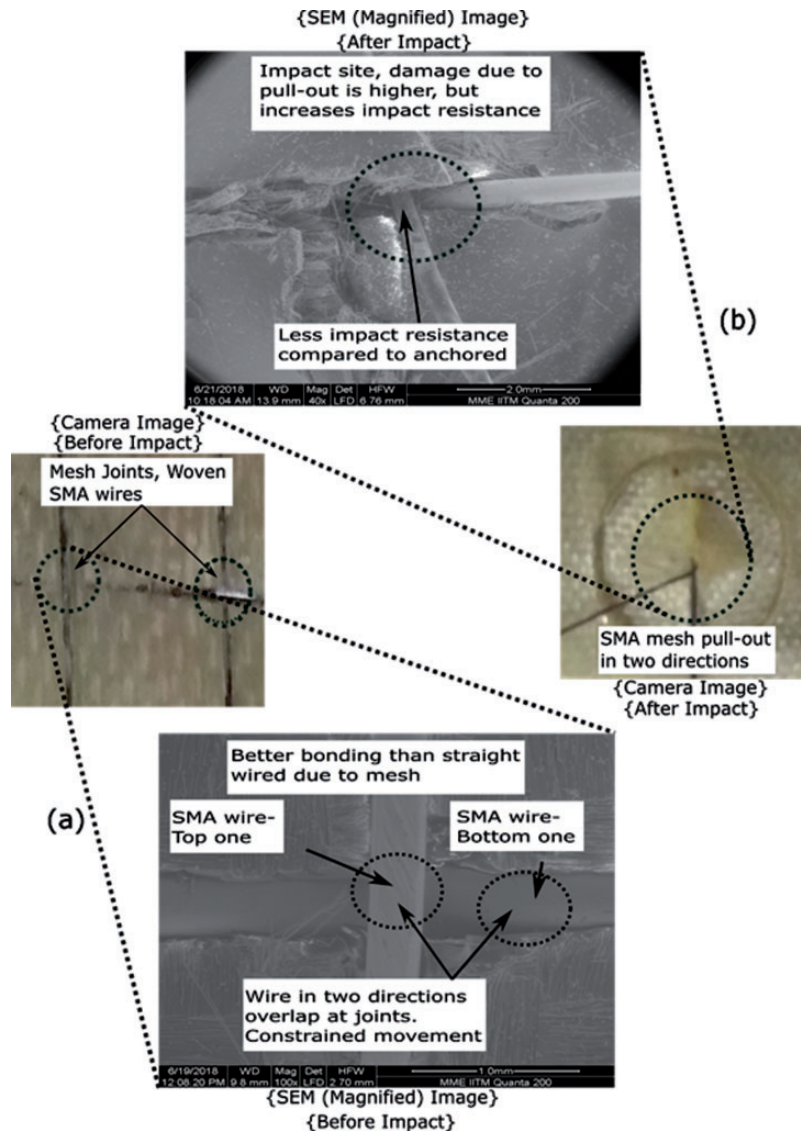
Figure 15. Meshed SMA-embedded patch repaired specimen showing (a) interaction between the wire and the matrix before impact and (b) damage modes after impact at the impact site using camera and SEM images.

a compression load, the damaged specimens might be under high-stress concentration at the outside edge of the hole. The ultimate rupture of those specimens might be sudden and catastrophic.[32] All the repaired composite specimens depicted the ultimate rupture at the transverse borders of the hole normal to the direction of compressive loading (Figure 20(a–d)). For the parent glass/epoxy specimens repaired using normal GFRP patches, a larger amount of cohesive or adhesive failure (Figure 20(a)) between the parent laminate and patch surface can be noticed. In this case, the adhesive layer between parent/patch interfaces failed initially and hence resulted in complete separation of the patches from the parent surface. Critical progression of damage between the over-lap edges of the external patches to the central hole was largely owed to the

interface failure. The lack of broken glass fibers (i.e., nonappearance of fiber/matrix debonding) on the surface of separated external patches additionally supported the existence of the adhesive or cohesive failure (Figure 20(a)). On one instance lacking the obstruction from the patches, the damaged parent laminate at once depicted ultimate rupture at the area most destabilized by the central hole. The chronology of failure mechanisms is as following: high stresses occurred in the patched area as the damaged specimens were repaired using normal GFRP patches characterized with brittle and low elongation features; subsequently, high shear stresses were generated in the adhesive layer[32] and encouraged the complete separation of the patches with increasing load; and the ultimate rupture occurred almost instantly in the site most
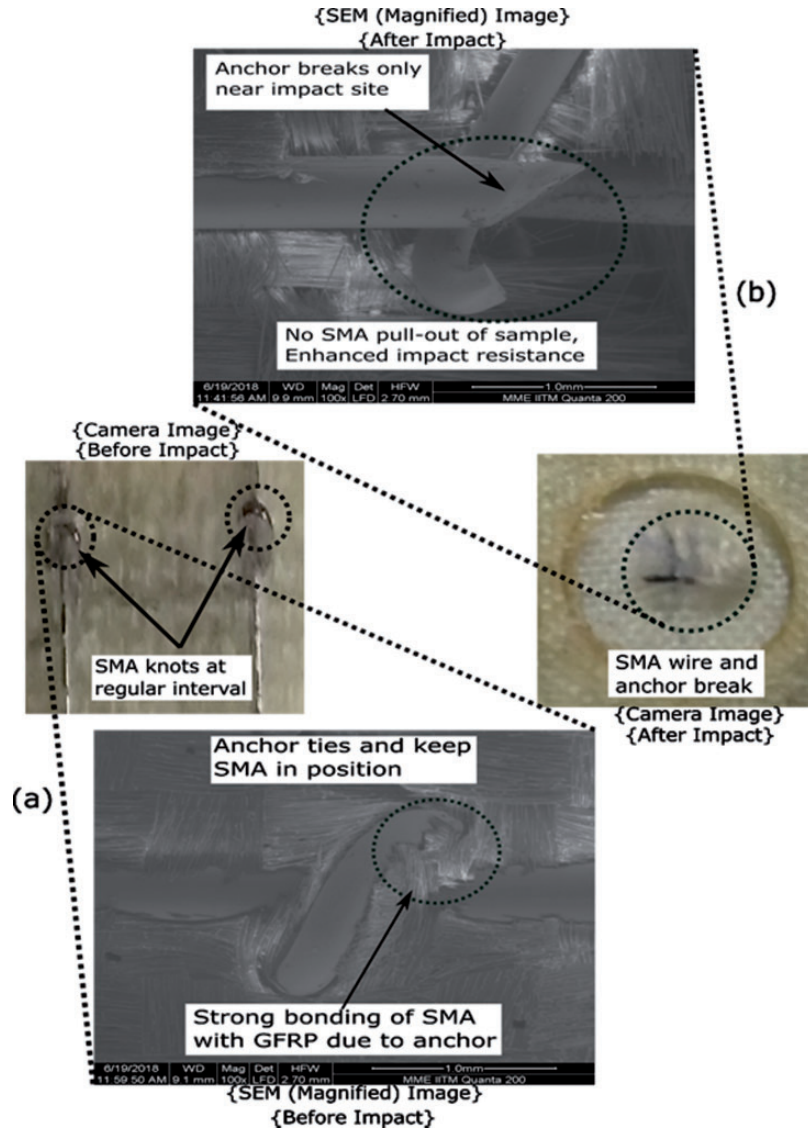
Figure 16. Anchored SMA-embedded patch repaired specimen showing (a) interaction between the wire and the matrix before impact and (b) damage modes after impact at the impact site using camera and SEM images.

destabilized by the central hole. This can clarify why the ultimate compressive load of high stiff normal specimens were lower than that of SMA-based specimens. An almost comparable failure profile was observed for the specimens repaired using straight-wired based external patches (Figure 20(b)). Although the ultimate rupture always occurred in the area most destabilized by the central hole, there was a small amount of fiber micro-buckling in the straight-wired patches which owed to the existence of fewer amounts of ductile SMA wires. This was because of the fact that the lower stiffness of the patch allowed the patch to deform along with the parent laminate.

The failure profile of the meshed and anchored SMA patch-based repaired specimens was completely

different (Figure 20(c,d)). It is clear that there was no substantial adhesive or cohesive damage among the patch–parent interface after rupture. The ultimate rupture had always taken place in the site most destabilized by the central hole, but the external patches were damaged and remained attached to the parent laminate. Instead, a small amount of adhesive or cohesive failure can be noticed near the overlap edges of the external patches. Adhesive or cohesive failure progression from the overlapping edge to the central hole is highly restricted by the anchored and meshed patches (Figure 20(c,d)). The patches encountered with fiber micro-buckling at the middle were mostly connected to the transverse edge of the central hole. This was a further indication for restricted progression of failure
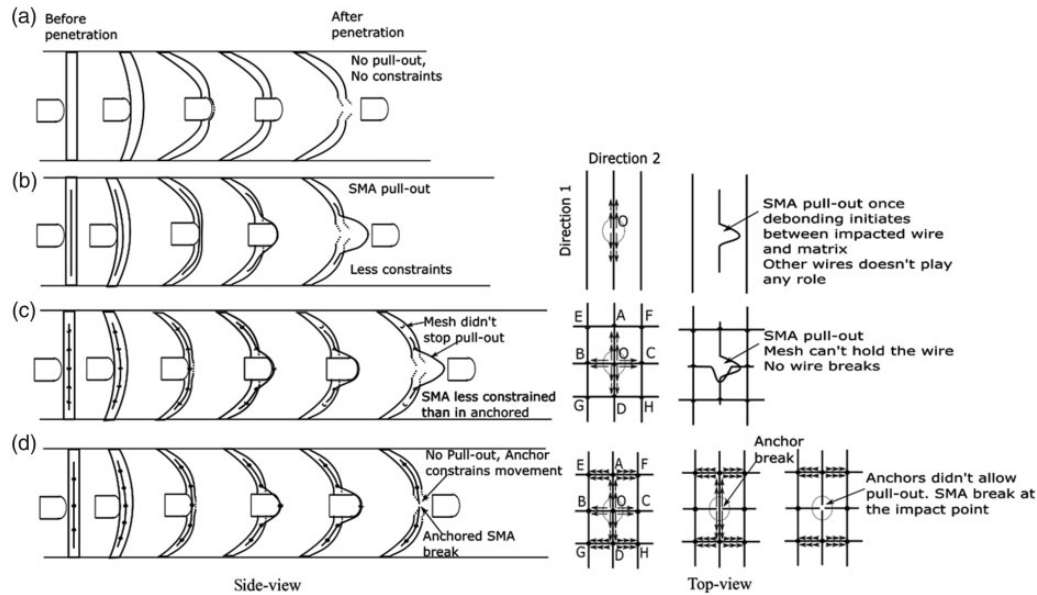
Figure 17. Schematic (side-view and top-view) diagram of the progression of damage in different repaired specimens: (a) GFRP, (b) straight-wired, (c) meshed, and (d) anchored impacted.
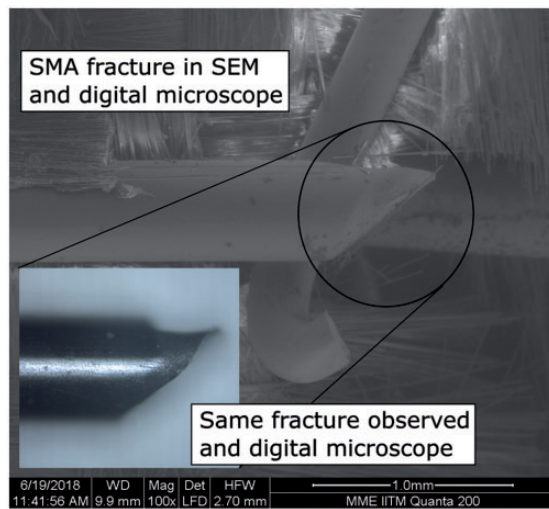

Figure 18. Fractured SMA wire at the point of impact.

Figure 19. Load vs. displacement curves for non-impacted specimens.

on the parent laminate. This failure profile signified that the rupture was the result of a concurrent progression of fracture in the patch overlap edge and the transverse edge of the central hole. The chronology of failure progression can be understood as the following: firstly, due to the shear stress occurred in the interface adhesive layer,[32] some micro-fracture have occurred in the overlapping edges of the patch and hence separated the patch at the overlapping edges; subsequently, microbuckling happened in the middle of the patches; afterward these two damaged areas progressed in the form
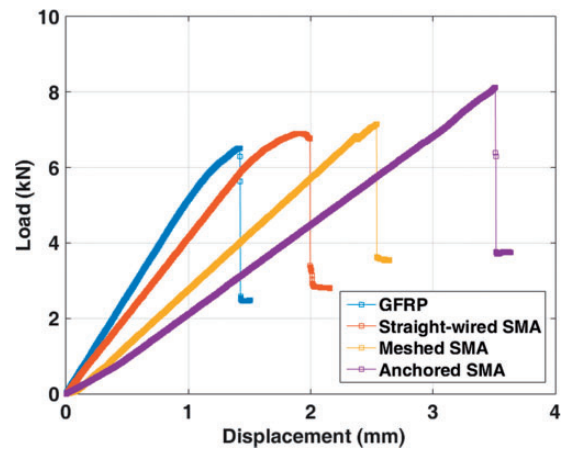
of adhesive or cohesive failure in the patch area; subsequently, as the lessening of the stress in the hole border was lower and redistribution of compression load into the destabilized zone was larger due to fiber micro-buckling, the specimen failed at the region most weakened by the central hole. Figure 20(c,d) depicts the fiber micro-buckling occurred in the parent laminate, initiating from the border of the hole across the width of the specimen, including a small amount of debonding/delamination and fiber micro-buckling of the external patches over and around the central hole. This might be accredited to the high ductile property offered
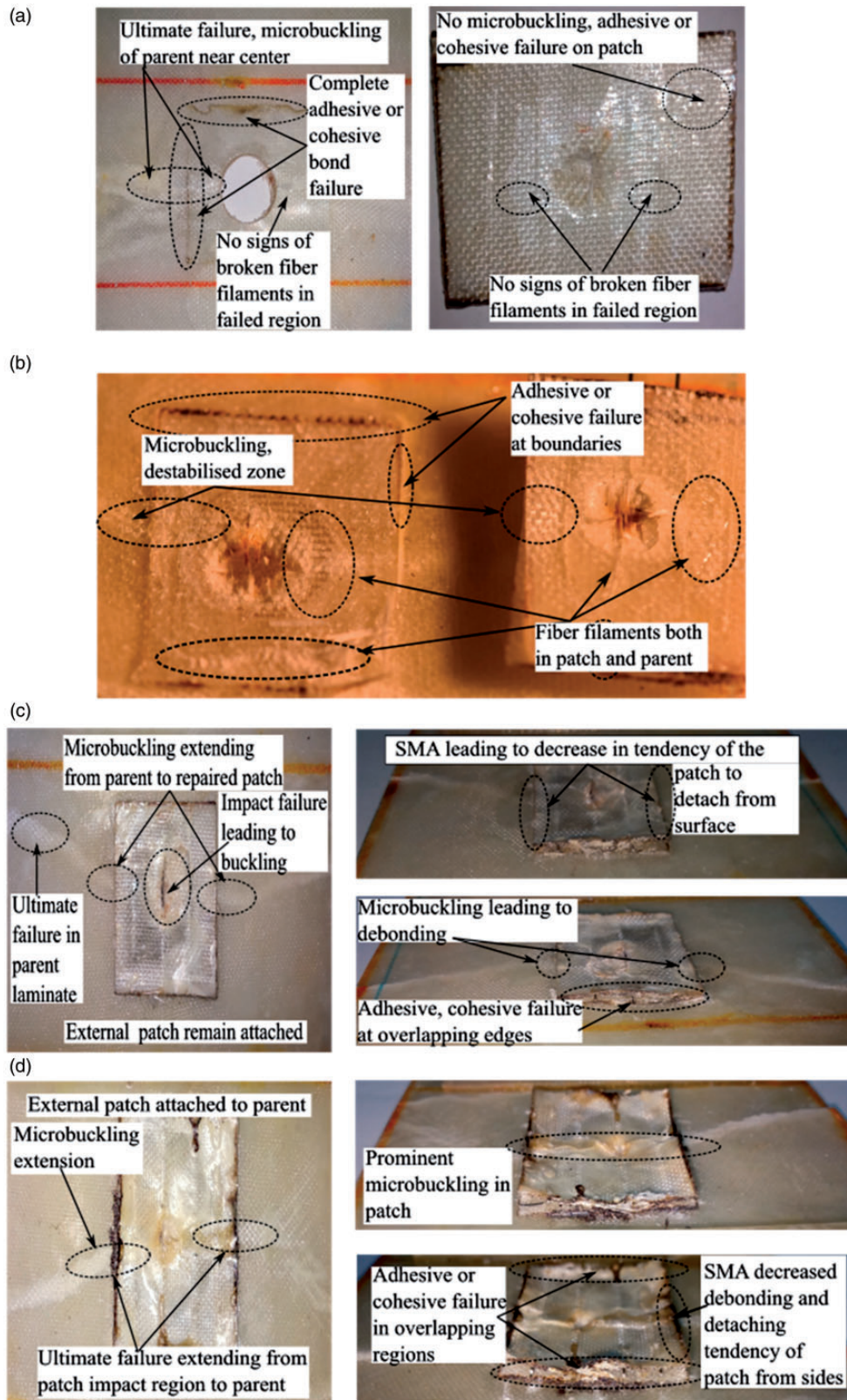
(a)

(b)

(c)

(d)

Figure 20. Photographic images of failure profile for various repaired specimens: (a) GFRP, (b) straight-wired, (c) meshed, and (d) anchored impacted.

by the high amount of SMA wires in meshed and anchored specimens under compressive load. The lower optimum stiffness provided by anchored and meshed external patch restricted the adhesive or cohesive failure unlike high stiff normal and straight-wired specimens (Figure 20). On the other hand, in the case of anchored specimens, the presence of higher amount of ductile SMA wires further provided excellent cooperation between the external patch and the parent laminate, unlike other SMA-based repaired specimens. These characteristics thus enhanced the overall load carrying capability, toughness, and ultimate displacement to the failure of anchored specimens.
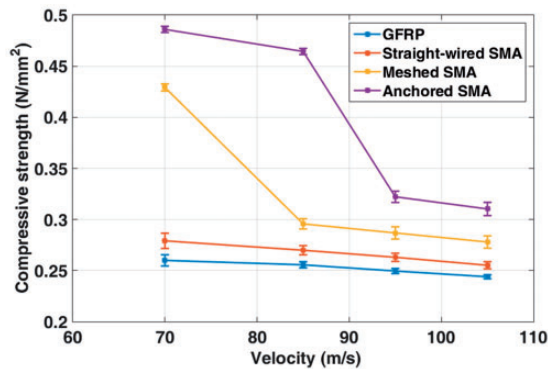

Figure 21. Compressive strength vs. velocity curve for different configurations of external patch repair.

Post-impact compression test. Figure 21 illustrates the ultimate compressive strength of impacted specimens at different velocities.

The increasing trend of damage for all repaired specimens with the rise in the impact velocity was well-matched by the reduction in the residual compressive properties (Table 4). In particular, the damage tolerance of all the repaired specimens reduced with increasing impact velocity. This owed to the reason that the impact load generated damage such as SMA pull-out, resin cracking, fiber/matrix debonding, interlaminar delamination, and fiber fracture in the specimens. However, it can be observed in Figure 17 that the trends of the ultimate compressive strength for impacted specimens (i.e. at 70, 85, 95 and 105 m/s) are same as that of the non-impacted ones. Since the initial stages of loading (i.e. from impact velocity of 70 to 105 m/s), normal and straight-wired specimens depicted almost saturated or moderately reducing behavior in terms of ultimate compressive strength (Figure 21). This was because the projectile critically penetrated the normal and straight-wired specimens at an impact velocity of 70 m/s itself (Figure 21(a,b)). After being impacted at a velocity of 85 m/s, the meshed specimens exhibited an abrupt decrement in the compressive strength (40% decrease at 85 m/s in comparison to 13% only at 70 m/s with respect to the non-impacted meshed specimens). Moreover, the percentage difference in compressive strength between straight-wired

Table 4. Compressive strength, modulus, and ultimate displacement at four velocities for different configurations.

Velocity (m/s)	Configurations	Ultimate displacement (mm)	Compressive strength (N/mm^2)	Compressive modulus (N/mm^2)
70	Glass/epoxy (GFRP)	1.50	0.26	26.00
	Independent straight wires	1.67	0.28	25.10
	Meshed straight wires	1.96	0.43	32.84
	Anchored straight wires	2.30	0.49	31.60
85	Glass/epoxy (GFRP)	1.60	0.26	24.00
	Independent straight wires	1.74	0.27	23.20
	Meshed straight wires	1.69	0.30	26.30
	Anchored straight wires	2.29	0.46	30.40
95	Glass/epoxy (GFRP)	1.63	0.25	23.30
	Independent straight wires	1.75	0.26	22.50
	Meshed straight wires	1.89	0.29	22.80
	Anchored straight wires	1.77	0.32	27.30
105	Glass/epoxy (GFRP)	1.66	0.24	22.70
	Independent straight wires	1.77	0.25	21.60
	Meshed straight wires	1.89	0.28	22.10
	Anchored straight wires	1.85	0.31	25.20

GFRP: glass fiber-reinforced polymer.

and meshed specimens was considerably lower (1.3% at 85 m/s) than at earlier impact velocity level (24.3% at 70 m/s), because, in this condition, the impactor highly penetrated through the thickness direction of the specimen. After being impacted at a velocity of 95 m/s, anchored specimens also exhibited an abrupt decrease in the compressive strength (Figure 17—40.3% at 95 m/s in comparison to 14% only at 85 m/s with respect to the non-impacted anchored specimens).

The percentage difference in ultimate compressive strength between meshed and anchored specimens was significantly lower than at impact velocity of 85 m/s (Figure 21—from 26% difference at 85 m/s to 1.5% at 95 m/s). The critical penetration occurred on the patch due to the impact event restricted effective transfer of compressive load from the parent laminate to the patch system at the damaged area. This was why the ultimate compressive load of anchored specimens nearly approached that of meshed specimens at an impact velocity of 95 m/s.

Conclusion

CAI tests were performed to study the impact response and damage tolerance of SMA-based external patch repaired glass/epoxy composite specimens. The experimental results observed from the CAI tests led to the following conclusions:

1. At all the impact velocities, normal and various SMA-based specimens were sorted from lower to higher energy absorption in the following order: normal < straight-wired < meshed < anchored. Normal, straight-wired, meshed, and anchored specimens offered ultimate absorbed energy of 16.4, 17.3, 23.5, and 32.3 J and depicted complete penetration at an impact velocity of 70, 70, 85, and 95 m/s, respectively.
2. Among various SMA-based specimens, anchored specimens were the only one to fail at higher impact velocity with a display of local elongation until SMA fractured. All other specimens containing SMA wires showed a considerable pull-out and debonding of SMA from the matrix.
3. Anchored specimens can be considered as a combination of meshed specimens with knots. These meshes distribute the impact load and were able to restrict the penetration of projectile and delayed the critical fiber fracture, unlike the normal and straight-wired specimens. The knots further strengthened the GFRP and SMA bond by providing anchors at the knotting points which controlled the premature pull-out of anchored SMA and further held it in a position.
4. Repairing the damaged glass/epoxy specimens using straight-wired, meshed and anchored external patches restored the compressive strength by 6.1%, 13.8%, and 25%, respectively, in comparison to the conventional normal specimens at the non-impacted conditions.
5. Anchored specimens presented a better post-impact compression response owing to the higher impact resistance at different impact velocities. The percentage reduction in the compressive strength came out to be the least for the anchored specimens (10% and 14% decrease at 70 and 85 m/s) in comparison to all the other configurations (39.3% and 41.3% for straight wired and 13% and 40% for meshed configuration at 70 and 85 m/s) with respect to the non-impacted specimens.

ORCID iD

G Balaganesan https://orcid.org/0000-0002-3867-6116
A Arockirajan https://orcid.org/0000-0002-2823-0217

References

1. Grabovac I and Whittaker D. Application of bonded composites in the repair of ships structures – a 15-year service experience. *Compos Part A* 2009; 40: 1381–1398.
2. Baker A. Bonded composite repair of fatigue-cracked primary aircraft structure. *Compos Struct* 1999; 47: 431–443.
3. McGeorge D, Echtermeyer AT, Leong KH, et al. Repair of floating offshore units using bonded fibre composite materials. *Compos Part A* 2009; 40: 1364–1380.
4. Kwon YW and Hall BL. Analyses of cracks in thick stiffened plates repaired with single-sided composite patch. *Compos Struct* 2015; 119: 727–737.
5. Bhatia GS, Andrew J and Arockiarajan A. Experimental investigation on compressive behaviour of different patch - parent layup configurations for repaired carbon/epoxy composites. *Journal of Composite Materials* 2019. DOI: 10.1177/0021998318822706.

6. Katnam KB, Da Silva LFM and Young TM. Bonded repair of composite aircraft structures: a review of scientific challenges and opportunities. *Prog Aerospace Sci* 2013; 61: 26–42.

7. Caminero MA, Pavlopoulou S, Lopez-Pedrosa M, et al. Analysis of adhesively bonded repairs in composites: damage detection and prognosis. *Compos Struct* 2013; 95: 500–517.

8. Andrew JJ, Srinivasan SM and Arockiarajan A. The role of adhesively bonded super hybrid external patches on the impact and post-impact response of repaired glass/epoxy composite laminates. *Compos Struct* 2018; 184: 848–859.

9. Andrew JJ, Arumugam V and Santulli C. Effect of post-cure temperature and different reinforcements in adhesive bonded repair for damaged glass/epoxy composites under multiple quasi-static indentation loading. *Compos Struct* 2016; 143: 63–74.

10. Andrew JJ and Arumugam V. Effect of patch hybridization on the tensile behavior of patch repaired glass/epoxy composite laminates using acoustic emission monitoring. *Int J Adhes Adhesives* 2017; 74: 155–166.

11. Xiaoquan C, Baig Y, Renwei H, et al. Study of tensile failure mechanisms in scarf repaired CFRP laminates. *Int J Adhes Adhesives* 2013; 41: 177–185.

12. Jefferson AJ, Arumugam V and Nath Dhakal H. 2 – Overview of different damage and common repair methods in composite laminates. In: Jefferson AJ, Arumugam V and Nath Dhakal H (eds) *Repair of polymer composites*. Cambridge: Woodhead Publishing, 2018, pp.45–95. Woodhead Publishing Series in Composites Science and Engineering. Available at: https://doi.org/10.1016/B978-0-08-102263-4.00002-8.

13. Madani K, Touzain S, Feaugas X, et al. Numerical analysis for the determination of the stress intensity factors and crack opening displacements in plates repaired with single and double composite patches. *Comput Mater Sci* 2008; 42: 385–393.

14. Kwon YW, Lee WY, McGee AS, et al. Analytical model for prediction of reduced strain energy release rate of single-side-patched plates. *Appl Compos Mater* 2013; 20: 1321–1339.

15. Belhouari M, Bouiadjra BB, Megueni A, et al. Comparison of double and single bonded repairs to symmetric composite structures: a numerical analysis. *Compos Struct* 2004; 65: 47–53.

16. Andrew JJ, Arumugam V, Ramesh C, et al. Quasi-static indentation properties of damaged glass/epoxy composite laminates repaired by the application of intra-ply hybrid patches. *Polym Testing* 2017; 61: 132–145.

17. Nallathambi AK, Doraiswamy S, Chandrasekar AS, et al. A 3-species model for shape memory alloys. *Int J Struct Changes Solids* 2009; 1: 149–170.

18. Verma L, Sivakumar SM and Vedantam S. Homogenization and improvement in energy dissipation of nonlinear composites. In: *Behavior and mechanics of multifunctional materials and composites 2016*. Vol 9800, Washington, DC: International Society for Optics and Photonics, 2016, p.980019.

19. Pappadà S, Gren P, Tatar K, et al. Mechanical and vibration characteristics of laminated composite plates embedding shape memory alloy superelastic wires. *J Mater Eng Perform* 2009; 8: 531–537.

20. Shen C, Wu Z, Gao Z, et al. Impact protection behavior of NiTi shape memory alloy wires. *Mater Sci Eng A* 2017; 700: 132–139.

21. Paine JS and Rogers CA. The response of SMA hybrid composite materials to low velocity impact. *J Intell Mater Syst Struct* 1994; 5: 530–535.

22. Wu Y, Wu Y, Wang Y, et al. Study on the response to low-velocity impact of a composite plate improved by shape memory alloy. *Acta Mech Solida Sin* 2007; 20: 357–362.

23. Paine JS and Rogers CA. Shape memory alloys for damage-resistant composite structures. In: *Active materials and smart structures*. Vol 2427, San Diego, CA: International Society for Optics and Photonics, 1995, pp.358–372.

24. Meo M, Marulo F, Guida M, et al. Shape memory alloy hybrid composites for improved impact properties for aeronautical applications. *Compos Struct* 2013; 95: 756–766.

25. Angioni SL, Meo M and Foreman A. Impact damage resistance and damage suppression properties of shape memory alloys in hybrid composites – a review. *Smart Mater Struct* 2010; 20: 013001.

26. Shen C, Wu Z, Gao Z, et al. Impact protection behavior of NiTi shape memory alloy wires. *Mater Sci Eng A* 2017; 700: 132–139.

27. Tsoi KA, Stalmans R, Schrooten J, et al. Impact damage behaviour of shape memory alloy composites. *Mater Sci Eng A* 2003; 342: 207–215.

28. Murkute V, Gupta A, Thakur DG, et al. Improvisation of interfacial bond strength in shape memory alloy hybrid polymer matrix composites. *Procedia Mater Sci* 2014; 6: 316–321.

29. Caminero MA, García-Moreno I and Rodríguez GP. Experimental study of the influence of thickness and ply-stacking sequence on the compression after impact strength of carbon fibre reinforced epoxy laminates. *Polym Testing* 2018; 66: 360–370.

30. Andrew JJ, Arumugam V, Bull DJ, et al. Residual strength and damage characterization of repaired glass/epoxy composite laminates using AE and DIC. *Compos Struct* 2016; 152: 124–139.

31. Andrew JJ, Arumugam V, Saravanakumar K, et al. Compression after impact strength of repaired GFRP composite laminates under repeated impact loading. *Compos Struct* 2015; 133: 911–920.

32. Rivallant S, Bouvet C, Abdallah EA, et al. Experimental analysis of CFRP laminates subjected to compression after impact: the role of impact-induced cracks in failure. *Compos Struct* 2014; 111: 147–157.

33. Jefferson Andrew J and Arumugam V. Effect of patch hybridization on the compression behavior of patch repaired glass/epoxy composite laminates using acoustic emission monitoring. *Polym Compos* 2018; 39: 1922–1935.

34. Petit S, Bouvet C, Bergerot A, et al. Impact and compression after impact experimental study of a composite laminate with a cork thermal shield. *Compos Sci Technol* 2007; 67: 3286–3299.

35. Xie W, Zhang W, Kuang N, et al. Experimental investigation of normal and oblique impacts on CFRPs by high velocity steel sphere. *Compos Part B* 2016; 99: 483–493.

36. Andrew JJ, Srinivasan SM and Arockiarajan A. Influence of patch lay-up configuration and hybridization on low velocity impact and post-impact tensile response of repaired glass fiber reinforced plastic composites. *Journal of Composite Materials* 2019; 53: 3–17.

37. Potti SV and Sun CT. Prediction of impact induced penetration and delamination in thick composite laminates. *Int J Impact Eng* 1997; 19: 31–48.

38. Lee SR and Sun CT. A quasi-static penetration model for composite laminates. *J Compos Mater* 1993; 27: 251–271.

39. Lee SW and Sun CT. Dynamic penetration of graphite/epoxy laminates impacted by a blunt-ended projectile. *Compos Sci Technol* 1993; 49: 369–380.